RESEARCH ARTICLE | MARCH 27 2025

Wind pressure characteristics of a short circular cylinder in supercritical regime using a novel force measurement method

Ying Chang (常颖) ; Lin Zhao (赵林) ; Yangzhao Liu (刘仰昭); Haili Liao (廖海黎); Yaojun Ge (葛耀君)

Physics of Fluids 37, 035206 (2025)
https://doi.org/10.1063/5.0256996

Physics of Fluids ARTICLE pubs.aip.org/aip/pof

Wind pressure characteristics of a short circular cylinder in supercritical regime using a novel force measurement method

Cite as: Phys. Fluids **37**, 035206 (2025); doi: 10.1063/5.0256996
Submitted: 8 January 2025 · Accepted: 11 February 2025 ·
Published Online: 27 March 2025

Ying Chang (常颖),[1] Lin Zhao (赵林),[2,a)] Yangzhao Liu (刘仰昭),[3] Haili Liao (廖海黎),[4] and Yaojun Ge (葛耀君)[2]

AFFILIATIONS

[1]Institute for Disaster Management and Reconstruction, Sichuan University–Hong Kong Polytechnic University, Chengdu 610207, China
[2]State Key Laboratory of Disaster Reduction in Civil Engineering, Tongji University, Shanghai 200092, China
[3]Department of Civil Engineering, Sichuan University, Chengdu 610065, China
[4]Southwest Jiaotong University, Chengdu 611756, China

[a)]**Author to whom correspondence should be addressed:** zhaolin@tongji.edu.cn

ABSTRACT

The pressure distribution around a cylinder is one of the classical aerodynamic problems involving Reynolds number (Re) effects. This paper presents the development of a novel distributed synchronous force measurement system, which experimentally investigates the effects of surface roughness and incoming turbulence on a short cylinder model with a diameter of 5 m under a supercritical regime ($Re = 2 \times 10^6$, 3.5×10^6). The study indicates that both surface roughness and incoming turbulence significantly alter the pressure distribution, albeit through distinct mechanisms. Roughness disrupts large-scale vortices, leading to distortions in the fluctuating wind pressure. The characteristic turbulence of the flow around a cylinder in the uniform flow is overshadowed by the characteristics of the incoming turbulence, which, in turn, affects the wind pressure distribution characteristics, particularly the fluctuating wind pressure. This turbulence effect is also mitigated by higher roughness. In current structural designs, the Re effect is typically approximated by attaching roughness strips to scaled models, while distortions in the fluctuating wind pressure due to high roughness are commonly neglected. Based on the statistical characteristics of wind pressure time series, it can be inferred that surfaces with high roughness significantly reduce the influence range of large-scale structural vortices by a factor of 6–10. This implies that when simulating the Reynolds effect by adding surface roughness to scaled models, distortions in the fluctuating wind pressure curve may occur, necessitating careful verification of the results obtained from the roughness model on the scaled model.

I. INTRODUCTION

The pressure distribution characteristics around a circular cylinder are one of the classical issues of bluff body aerodynamics, and the classic theory provides a fundamental support in the wind design of structures. Reynolds number (Re), defined as the ratio of inertial force to viscous force, has a great influence on the flow around a circular cylinder. Zdravkovich (1997) studied and summarized the flow transition process with Re and proposed a detailed division system to describe flow field regimes with distinct characteristics, such as subcritical (TrSL3), pre-critical (TrBL0), one separation bubble (TrBL1), two separation bubbles (TrBL2), supercritical (TrBL3), and transcritical (TrBL4). At higher Reynolds numbers in the supercritical regime, separation bubbles break, the low drag coefficient (C_D) caused by the double separation bubble starts to increase slowly, and the base coefficient (C_{pb}) becomes uneven. Additionally, due to the development of 3D characteristics of the flow field, the periodic vortex shedding disappears. Roshko (1961) found for the first time that the periodic vortex shedding reappeared at a higher Re, which is called the transcritical regime.

The flow around a circular cylinder is very sensitive to small disturbances, such as surface scratch or non-uniformity of incoming flow, which often leads to evident differences in test results under different experimental conditions with similar Re (Schewe, 1983). In addition, some important parameters will significantly affect the flow field and structural loads, such as imperfectly circular cross sections (Abdelhadya and Wood, 2021), surface roughness (McTavish *et al.*,

2020), and incoming turbulence (Maryami *et al.*, 2020; Chang *et al.*, 2022). This leads to the limitation of classical theory in wind design for practical structures, which are immersed in the atmospheric boundary layer exposed to incoming turbulence, and the surface of which is not perfectly smooth. Bearman and Morel (1983) identified three basic mechanisms for the influence of incoming turbulence on flows around bluff bodies: accelerated transition to turbulence in the shear layer, enhanced mixing and entrainment, and distortion of incoming turbulence. For the engineering design, these three mechanisms lead to load changes, including smoother curves of C_D (Surry, 1972; Khabbouchi *et al.*, 2014; and Maryami *et al.*, 2020), higher fluctuating wind pressure (C_p'), and non-Gaussian characteristics (Chang *et al.*, 2022), earlier reappearance of regular vortex shedding (Zan, 2008). Moreover, Chang *et al.* (2022) found that turbulence effects have a certain Re effect, meaning that the effect varies at different Re. Surface roughness also has a significant effect on flow around a circular cylinder. Achenbach (1968) and Achenbach and Heinecke (1981) studied the influence of roughness and found that surface roughness makes the boundary layer transition occur earlier. With the increase in surface roughness, the Re effect for each regime would be re-illustrated in lower Re, and the boundaries between critical, supercritical, and transcritical regimes become blurred until each Re regime is merged. For compensating the Re effect of surface aerodynamic pressure distribution, the characteristics of surface roughness can be used to simulate the flow fields in the supercritical regime by adjusting model surface roughness. Zhao *et al.* (2022) utilized this characteristic to carry out the cooling tower group test in the wind tunnel, taking the same mean wind pressure distribution with the Chinese Code GB/T 50102-2014 (2014) as the compensation target of the Re effect. Chen *et al.* (2013) used a scaled chimney model with model surface roughness, and the mean wind pressure distribution of which is consistent with the full-scale measurement results. However, the influence of surface roughness on fluctuating pressure has not been well clarified, which may result in the inadequacy of Reynolds number compensation methods for refined wind pressure results.

As mentioned earlier, as the primary factors affecting wind pressure distribution, both turbulence and roughness effects exhibit a distinct Reynolds number dependency. The Reynolds number Re is defined as $\mathrm{Re} = \rho UL/\mu$, in which ρ is the air density, U is the wind speed, L is the characteristic length, and μ is the air motion viscosity coefficient. Re is mainly related to the model's dimensions and wind speed. Increasing the model size is one of the important means to increase the Reynolds number. However, when the model size is large, the length of tubes that are used in a pressure measurement system will increase significantly, leading to serious signal amplitude and phase distortion problems. There are generally two methods to solve the signal distortion problem of the pressure measurement system: (1) utilizing restrictors (Irwin *et al.*, 1979; Holmes and Lewis, 1987a; 1987b) and (2) correcting distorted signals by theoretical models (Bergh and Tijdeman, 1965; He *et al.*, 2019; Kay *et al.*, 2020; and Pallas *et al.*, 2024). The use of restrictors was more frequent in the early stages, and currently, theoretical models are mainly used to correct the pressure measurement data. However, both methods have certain shortcomings, such as not being suitable for longer pipelines (Irwin *et al.*, 1979), or the theoretical derivation involves many assumptions, with a large number of model parameters and complex modeling (Pallas *et al.*, 2024). This leads to difficulties in obtaining wind pressure data in large structural model tests.

The utilization of balances for directly acquiring aerodynamic forces on a cylinder model is one of the commonly employed measurement techniques. By integrating the entire model onto a multicomponent balance, it is feasible to directly measure the aerodynamic forces in various directions (Zan, 2008; Ma *et al.*, 2019b). In the context of the emerging hybrid experiments, in recent years, high-precision balances are reasonably adopted (Hwang *et al.*, 2024). They can more precisely determine the aerodynamic forces on models with complex geometries and more directly convey the results to hybrid simulation systems. In certain dynamic experiments, balances with higher precision and smaller ranges have been engineered and positioned between the primary skeletal structure of the model and its lightweight outer shell (Zhu *et al.*, 2013). The lightweight shell ensures minimal inertial forces, thereby allowing the use of small-range, high-precision balances to more accurately capture the aerodynamic forces. This aerodynamic force acquisition technology has also been applied in the establishment of numerical twin models that are integrated with computational fluid dynamics simulations (Li *et al.*, 2024). However, traditional force measurement methods, which often relied on a single or just a few balances, were at a distinct disadvantage compared to pressure tubing systems when it came to the synchronized acquisition of aerodynamic forces at multiple structural measurement points.

To address the shortcomings of long tube pressure measurement systems and traditional balance measurement systems, a novel distributed synchronous force measurement system has been developed in the current attempt. This system utilizes 20 synchronized balances to directly acquire force signals at specific local positions on the large-scale model, thereby circumventing the signal distortion issues arising from excessively long pressure tubes. Utilizing this experimental setup, the present study investigates the influence of free-stream turbulence and surface roughness on the flow around a short circular cylinder under high Re conditions ($\mathrm{Re} = 2 \times 10^6$, 3.5×10^6). This work provides a detailed explanation of the impact of turbulence and roughness on the wind pressure distribution around the short circular cylinder in a supercritical Re regime, and the vortex characteristics and influencing mechanisms were analyzed through statistical feature analysis. The results offer potential assistance for engineering design to meet the needs of more precise wind resistance design for actual large-scale engineering structures.

II. EXPERIMENTAL SETUP

A. Large-scale model and distributed synchronous force measurement system

In order to reproduce the flow field around a cylinder with higher Reynolds numbers in an atmospheric boundary layer wind tunnel, a short circular cylinder model with a diameter of 5 m was employed. A distributed synchronous force measurement system was utilized, comprising 20 three-component high-frequency dynamic balances to capture detailed force data. The schematic diagram of the model installation is shown in Fig. 1. The circular model is a short column with a height of 1.4 m and an aspect ratio of 0.28. Its upper end is covered with a circular end plate with a diameter of 8 m. To ensure sufficient rigidity, the upper surface of the end plate is braced by eight aluminum steel tubes, and corresponding support components are also placed inside the model, minimizing the interference of end plate vibrations to the greatest extent possible. The force-measuring section is set in the middle of the model elevation. Considering the symmetry

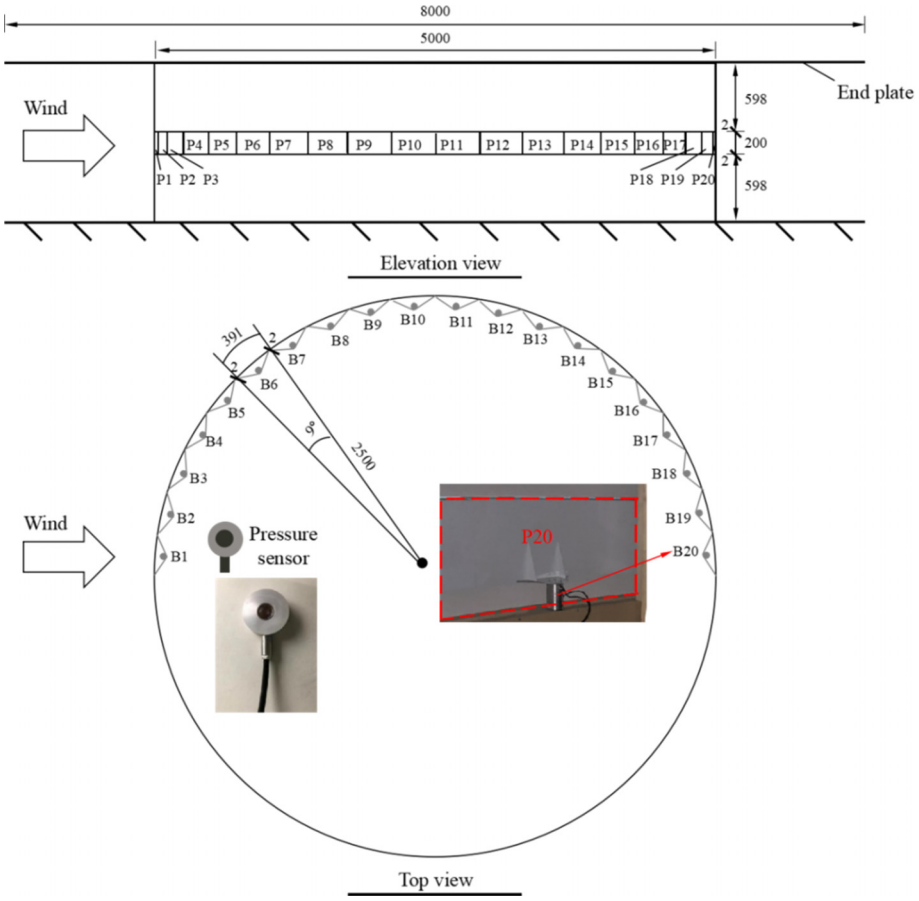

FIG. 1. Diagram of the short cylindrical model and force measurement system (unit: mm).

of the flow field in the supercritical regime, 20 force balances were used to measure the wind pressure within the range of 0°–180°. Each balance is connected to a force plate, which is a curved panel occupying a central angle range of 9°. The 20 force plates are numbered in order of position as P1, P2, …, P20, and the corresponding balance number is B1, B2, …, B20. The force-measuring section and both compensating sections are fabricated from the same material, ensuring the continuity of material and curvature on the cylindrical surface. To avoid any direct contact and distribution, each force plate is 0.2 m high with a 2-mm gap between the upper and lower compensation sections and the adjacent ones. Therefore, only the forces on each force plate were measured in the test. The three-component balance is designed to measure forces in both the x and y directions, as well as the moment of force (torque) about the z-axis, with measuring ranges of 25 N for the x and y directions and 4 N·m for the z-direction. Force data were recorded using a 60-channel data acquisition unit. The sampling frequency is 100 Hz.

Zhu *et al.* (2013) designed a dynamic aerodynamic measurement method for bridge cross sections, which measured the overall dynamic force of a bridge segment model using four balances. The high-precision vortex-induced force signals were successfully obtained by setting a 2-mm gap between the side and middle coat segments. Yan *et al.* (2025) used a six-component high-frequency force balance to measure aerodynamic forces of a stationary road vehicle model on the sectional truss girder bridge model. The balance connecting the road vehicle model is placed underneath the bridge deck through an empty square hole, and the 6 aerodynamic coefficients of the road vehicle are successfully obtained, indicating that this testing method has good feasibility. To evaluate the potential airflow between the plates, a dynamic wind pressure sensor was installed inside the model near the locations of balances B1 and B2 to monitor the internal wind pressure variations, as shown in Fig. 1. The gap at this location faces directly into the oncoming flow and is most likely to generate a jet flow through the gap. The pressure fluctuations measured here can be used to infer the intensity of the airflow between the plates. Figure 2 presents the results of the internal pressure time history against the reference dynamic pressure under various wind speeds. As can be seen from Fig. 2(a), under the condition of no wind and stable internal pressure, there is a certain degree of fluctuation in the sensor signal, and the root mean square is approximately 4.49. It is caused by environmental noise and the signal fluctuation of the sensor itself. With the increase in wind speed, the amplitude of the signal fluctuation shows a slight increase, reaching 3.53 at 6 m/s and 6.71 at 10 m/s, approximately 0.15 and 0.11 of the dynamic pressure reference value. Taking into account the inherent fluctuation characteristics of the signal, it is reasonable to conclude that the 2 mm gaps between the force plates have a minimal influence on the internal flow field. Moreover, it can be assumed that the internal pressure remains stable throughout the experiment.

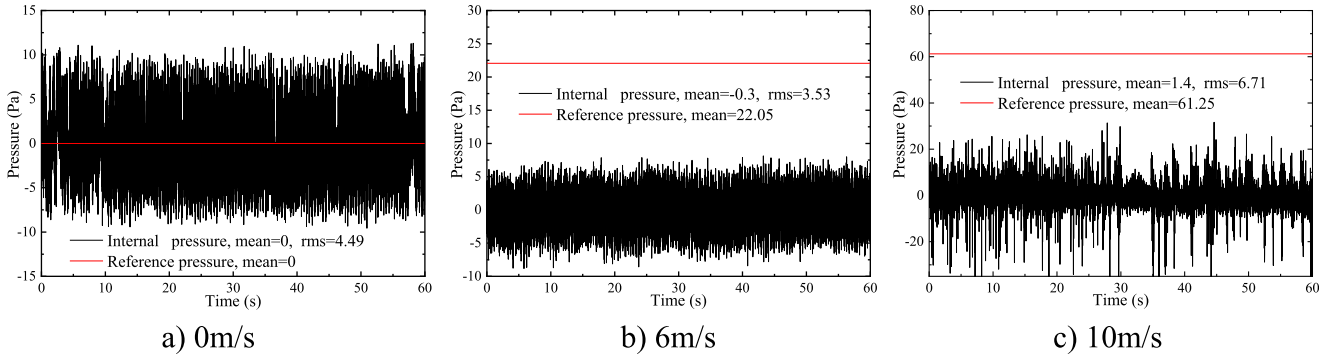

FIG. 2. Internal pressure fluctuation time history vs the reference dynamic pressure.

The specific connection method between the force plate and the balance, as well as the coordinate system of the balance, is shown in Fig. 3. The balance is connected to the center of the force plate via a connector. For the force plate–balance system at each position, the x-direction of the balance is parallel to the normal force at the center of the force plate. Since the panel is curved, the wind load on the force plate varies in direction and magnitude along the circumference of the model. Given that the force plate covers a small central angle, the wind load varies little at different positions on the force plate. In this work, the wind load on the force plate is equivalent to a resultant force perpendicular to the center of the force plate, which is parallel to the x-axis of the balance. Calibration of the force measurement system was performed before the test. Each three-component balance has a 3×3 calibration matrix consisting of nine calibration factors, to reflect the relationship between the applied forces and the normalized output voltages. The signals from 20 balances were amplified by their respective amplifiers, and synchronized signal acquisition was achieved using the same multichannel data acquisition unit and a computer.

According to the test results, the internal pressure is consistent with the external static pressure with small fluctuation. Therefore, the internal pressure is verified to be stable and uniform during the tests. Then, the force measured $F_{Balance}$ for each angle is

$$F_{Balance}(\theta) = F_{in}(\theta) - F_{out}(\theta), \tag{1}$$

where $F_{in}(\theta)$ is the inside force generated by the change of air pressure inside the model and $F_{out}(\theta)$ is the outside resultant force on the force measured plate. Due to the stable and balanced internal and external environmental pressures, the wind pressure coefficient C_p can be obtained directly as follows:

$$C_p(\theta) = (-F_{Balance})/(\rho U^2/2). \tag{2}$$

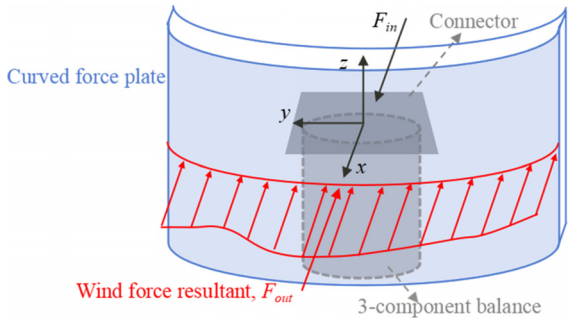

FIG. 3. Surface aerodynamic force measurement and calculation.

B. Wind tunnel system and working conditions

Wind tunnel experiments with the short circular cylinder model were conducted in the XNJD-3 wind tunnel at the Southwest Jiaotong University. The XNJD-3 wind tunnel is a boundary layer wind tunnel with the largest section size in the world. The working section is 36 m long, 22.5 m wide, and 4.5 m high. The wind tunnel power system is composed of four fans arranged in parallel with a diameter of 4.5 m. The maximum wind speed can reach 16.5 m/s with the flow field nonuniformity index $\delta U/U \leq 1.5\%$. The blocking ratio calculated according to the projected area of the circular model is 7%. Due to the lack of wind pressure distribution characteristics and parameter influences of flow around a circular cylinder in a supercritical regime, especially under the influence of surface roughness and incoming turbulence, the test would be of considerable value to clarify the corresponding issue, and it also meets the requirements of wind tunnel testing specification (JGJ/T 338-2014, 2014), which recommend the blocking ratio is <8%.

Circular cylinder model tests were performed in both smooth and turbulent incoming flows at two wind speeds, 6 and 10.5 m/s, corresponding to $\mathrm{Re} = 2 \times 10^6$ and 3.5×10^6, respectively. Smooth incoming flow refers to the flow in the unobstructed wind tunnel. The turbulent incoming flow was generated using 13 rectangular plates located 22 m upstream with four different widths (0.2, 0.3, 0.4, and 0.5 m), as shown in Fig. 4. Due to the diameter of the cylindrical model used, this time being 5 m and the lateral dimensions being wide, it is necessary to verify the turbulence uniformity within a wide range of the flow field spanwise. Before installing the model, the Cobra probes were used to measure the flow fields simultaneously at different positions in the x, y, and z directions, as shown in Figs. 4(a) and 4(b). The x–y–z coordinate is located at the turbulence generator section, with its origin located at a height of 0.7 m above the ground, which is consistent with the height of the force-measuring section center. x represents the streamwise distance, y is the vertical direction, and z is the horizontal direction. The flow characteristics of two points along the wind tunnel axis on the same cross section, vertically separated by 0.2 m and horizontally separated by 3 m, were tested simultaneously.

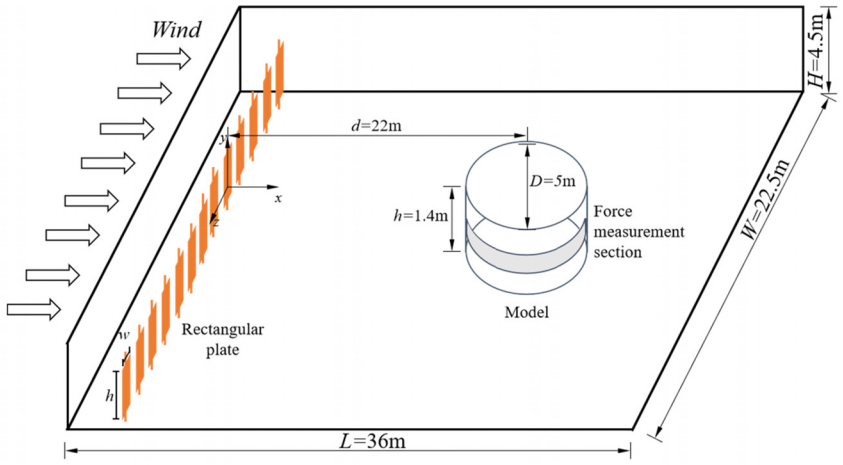

a) Experimental setup diagram

b) Rectangular plates and probe sensor

c) The model with smooth surface

d) The model with rough strips

FIG. 4. Diagram of measured model and turbulence generating plates in the XNJD-3 wind tunnel.

The turbulence intensity (I_u) can be calculated from $I_u = \sigma(u)/\overline{U}$, in which $\overline{U}$ is the mean wind speed and $\sigma(u)$ is the standard deviation of longitudinal fluctuating wind component u. The integral scale (L) measures the correlation distance of a flow process in terms of space or time. Adopting Taylor's hypothesis that the vortex is transmitted downstream at the average wind speed U without attenuation, the integral scale L_u^x (the u velocity component along the mainstream x) can be calculated through the mathematical integral of the autocorrelation function $R_u(\tau)$ as

$$L_u^x = \frac{U}{\sigma_u^2}\int_0^\infty R_u(\tau)d\tau. \tag{3}$$

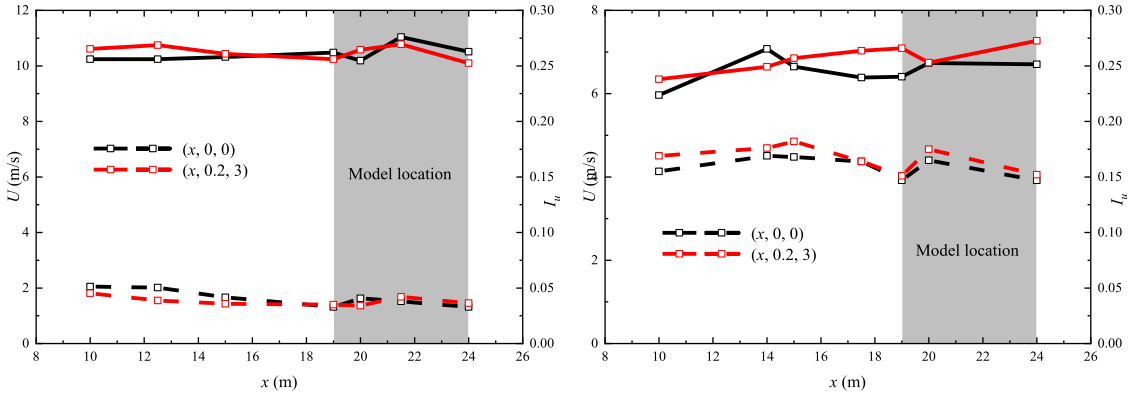

FIG. 5. Flow field test results (solid lines: mean wind speed; dashed lines: incoming turbulence).

TABLE I. Turbulence generation plate sizes and turbulence parameters (T1, T2, T3, and T4 refer to four different turbulence flow fields).

Turbulence	T1	T2	T3	T4
Plate width, w (cm)	20	30	40	50
Plate height, h (cm)	150	150	150	150
I_u (%)	4	7	10	15
L_u^x (cm)	30	50	50	60

The integral upper limit is taken as when $R_u(\tau) = 0.05\sigma_u^2$ (Flay and Stevenson, 1988). The $\overline{U}$ and I_u of the minimum and maximum turbulence intensities along the flow direction in the wind tunnel are shown in Fig. 5, and the parameters of the turbulent flow field are shown in Table I. The turbulent flow field exhibits satisfactory uniformity in the downwind and spanwise directions within the location of the models. This paper mainly investigates the influence of turbulence intensity and surface roughness, and the results show that the flow field has acceptable homogeneity about turbulence intensity level in the downwind and spanwise directions within the location of the models, as shown in Fig. 5. Except for the mean horizontal wind speed U, the mean wind speeds in other two directions, V and W, are virtually zero. The typical spectrum at $U = 6$ m/s is shown in Fig. 6. The turbulent energy was evenly distributed in the low-frequency band without prominent peaks. Then, it gradually weakened in the high-frequency band, which is a typical broadband wind spectrum.

The roughness is simulated by attaching multilayer fiber strips on the surface of the model. The thickness and width of each layer of roughness strips are 5 and 20 mm, respectively. A total maximum of ten layers have been pasted, and the height k of roughness strips is 5–50 mm. According to the pressure test of a rigid model of gas tank structure carried out by Liu *et al.* (2022), when the net distance ratio (ratio of distance between rib edges and distance between rib centers) is <0.9, the C_p (mean wind pressure coefficient) and C_p' (fluctuating wind pressure coefficient) distribution of wind load on the surface of the gas tank almost do not change with the roughness. Therefore, this paper sets an equivalent roughness with a net ratio of 0.9, and the equivalent roughness, defined

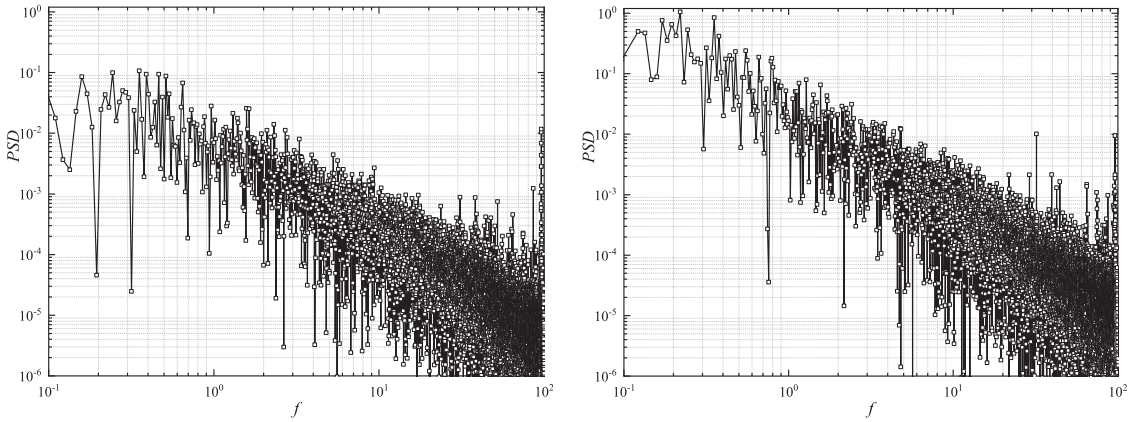

FIG. 6. PSD at $U = 6.7$ m/s for each turbulent flow.

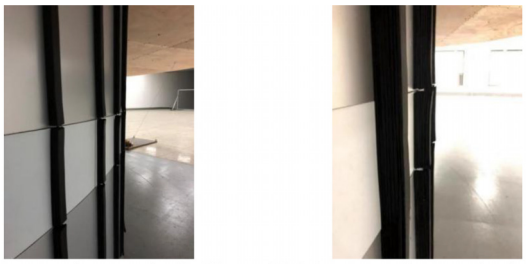

a) 4-layer roughness strip, k=20mm b) 8-layer roughness strip, k=40mm

FIG. 7. Roughness strips pasted on the model.

as the ratio of the height k of the roughness strip to the center distance s, ranges from 0 to 0.23, as shown in Fig. 7 and Table II.

III. EXPERIMENTAL RESULTS

A. Re effect for smooth short circular cylinder

Although only the wind pressure within the range of 0°–180° was measured in the tests, due to the symmetry of the flow field in the Re regime of TrBL3 and TrBL4, the C_p distribution within the range of 180°–360° can be simply obtained by the symmetry of 0°–180°. The C_p variation can be used to infer the corresponding flow characteristics. At the stagnation point, the wind speed is nearly zero, and C_p reaches its maximum value of 1. As the angle increases, the wind speed rises, while the wind pressure coefficient decreases. At the sides of the cross section, the wind speed is at its maximum, and C_p is at its minimum, defined as C_{pmin} and the corresponding angle as θ_{min}. As the angle further increases, the adverse pressure gradient causes the flow to separate. Afterward, it is the wake region. C_p in the wake region is relatively stable and significantly determines the value of the drag coefficient C_d. Therefore, C_p in the wake is defined as the base pressure Cpb. In this study, the separation location θ_{pb} is estimated as the angle at which the C_p curve slope reaches zero. The base pressure C_{pb} is calculated by averaging all the wind pressure coefficients in the wake region. The results are shown in Fig. 8 and compared with other experiments and field measurement results. The drag coefficient C_D and lift coefficient C_L are defined as

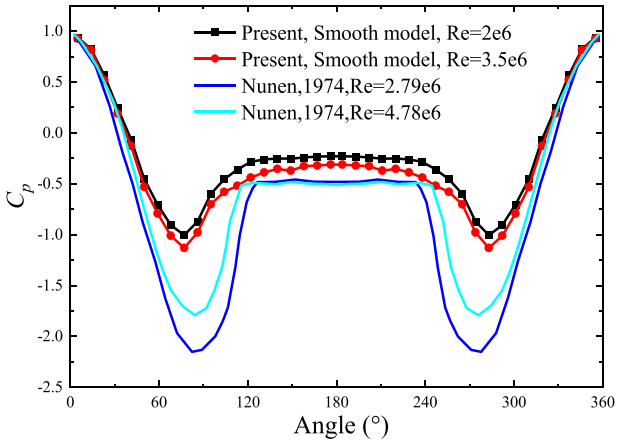

FIG. 8. Results and comparison of C_p distribution at typical Re.

$$C_D = F_D/\left(\rho U^2 D/2\right), \tag{4}$$

$$C_L = F_L/\left(\rho U^2 D/2\right), \tag{5}$$

where F_D and F_L refer to along wind force and crosswind force per unit length, respectively, and can be obtained by integrating the C_p curve. Figure 9 gives the results and comparison of a C_D at a typical Re regime.

According to the C_p distribution shown in Fig. 8, the present results have a certain difference with van Numen's (1974) experiments at similar Reynolds numbers. The main difference is that $|C_{pmin}|$ in this paper is small, around 1.0, while $|C_{pmin}|$ in van Numen's (1974) experiments is in the range of 1.5–2. The reasons causing this difference may include the following two aspects: (1) C_p distribution results at the same Re with similar parameters in TrBL3 can be quite different (Roshko, 1961; Jones *et al.*, 1969; and van Numer, 1974). The irregular three-dimensional transition of the free shear layer leads to a higher randomness of the flow field, and the unforeseeable rupture and fragmentation of the separation bubble can also lead to the different C_p distribution at different spanwise positions in the same experiment (Zdravkovich, 1997). It can be also seen in Fig. 9 that C_D at high Re is relatively discrete and distributed in a wide range. (2) The short

TABLE II. Parameters of roughness strips.

Model diameter, D (m)	$\overline{U}$ (m/s)	Re	Strip width, b (mm)	Strip number	Distance, s (mm)	Ratio, $(s-b)/s$	Strip height, k (mm)	Equivalent roughness, k/s
5.00	6.00, 10.5	$(2–3.5)\times10^6$	20.0	72	218.2	0.9083	0	0.00
							5	0.02
							10	0.05
							15	0.07
							20	0.09
							25	0.11
							30	0.14
							35	0.16
							40	0.18
							50	0.23

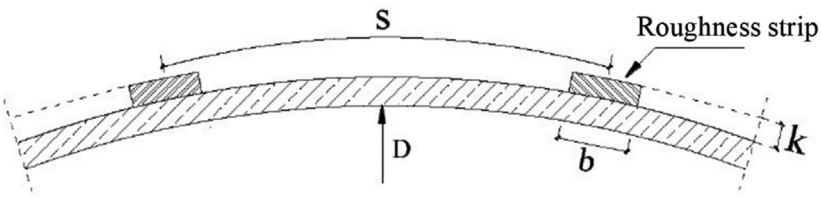

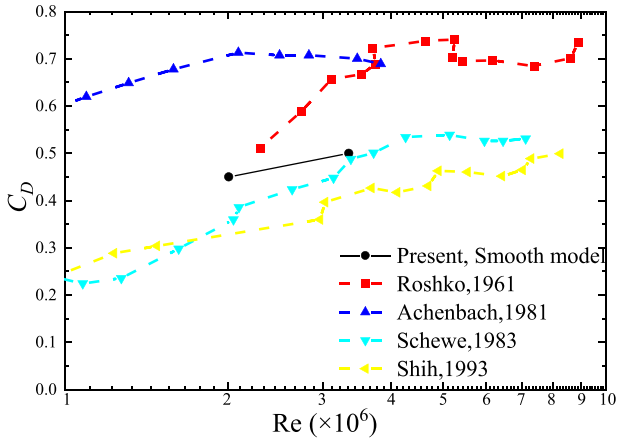

FIG. 9. Comparison of C_D variation at typical Re.

cylinder model is used in this work. Wang *et al.* (2012) experimentally found distinct differences from short cylinders with 3D effects. The vortices derived from column ends would induce downwash flows and interfere with the wake, and the base pressure C_{pb} increases. Liu *et al.* (2022) carried out wind tunnel tests on cylindrical storage tanks with four aspect ratios ($H/D = 0.2$–1.5) and found that as the H/D of the cylinder decreases, the Re effects are attenuated or even disappear gradually. Ma *et al.* (2019a) found that the end effect can be effectively eliminated by using appropriate end plates. On the other hand, the aforementioned studies are conducted in subcritical or critical regimes, and their applicability in supercritical regimes needs to be verified. In this study, the close agreement of C_{pb} with previous references suggests that the end plates remain effective in suppressing downwash even in the transcritical regime. Under these conditions, C_p distributions at both Reynolds numbers are remarkably similar. C_D exhibits a gradual increase with Reynolds number starting from 0.4, which is a characteristic value commonly observed at the onset of TrBL3, and this C_D value of 0.4 is insufficient to eliminate the separation bubble (Zdravkovich, 1997). Based on these observations, it is inferred that the Reynolds number range investigated for the short cylinder corresponds to the TrBL3 regime.

The wind pressure fluctuation C_p' defined as the standard deviation of the wind pressure time history and the power spectral density (PSD) is shown in Fig. 10. The distribution under two Re numbers is relatively similar. The C_p' distribution in the range of 80°–110° is large enough to form a high platform, while in other areas, C_p' is flat and small. With the increase in Re, C_p' increases slightly. The PSD represents the energy distribution in each frequency band, and its integral is the variance of the signal. The areas where the PSD amplitudes are extremely large and small are shown in black and white, respectively. There is obvious energy accumulation only in the area with large C_p', and both occur at low frequencies, such as $fD/U < 0.2$, which indicates the potential presence of a separation bubble.

The separation bubble represents the region between flow separation and reattachment. Beneath the separation bubble, the pressure variation is minimal. In the critical and supercritical regimes, laminar separation initially occurs, forming a separation bubble, followed by flow transition and turbulent separation. It is well established that for perfectly smooth cylinders, the transition location moves upstream along the cylinder surface with increasing Re. This movement gradually overtakes the flow separation location at high supercritical Reynolds numbers, continuing toward the stagnation point. This phenomenon explains why the separation bubbles progressively shrink, eventually bursting and disappearing at the end of the supercritical regime.

At $\mathrm{Re} = 2 \times 10^6$, as shown in Fig. 10(a), the PSD graph suggests that the separation bubble is located within the 90°–120° range. As Re increases to $\mathrm{Re} = 3.5 \times 10^6$, the bubble's coverage area decreases, and its position shifts closer to 90°. The observed changes in separation bubble position and size at two Reynolds numbers align with this principle, supporting again that the regime transition falls between TrBL2 and TrBL3.

B. Surface roughness effect

Figure 11 gives C_p distributions under different equivalent roughness at two Re numbers. It can be seen that C_p distributions of smooth and rough cylinders are quite different. The minimum mean wind pressure C_{pmin} of the smooth model is about −1.0, and that of the rough cylinder is larger than −1.0. θ_{min} and θ_{pb} both move upstream. So the wake region becomes wider. Figure 11 shows the variation of

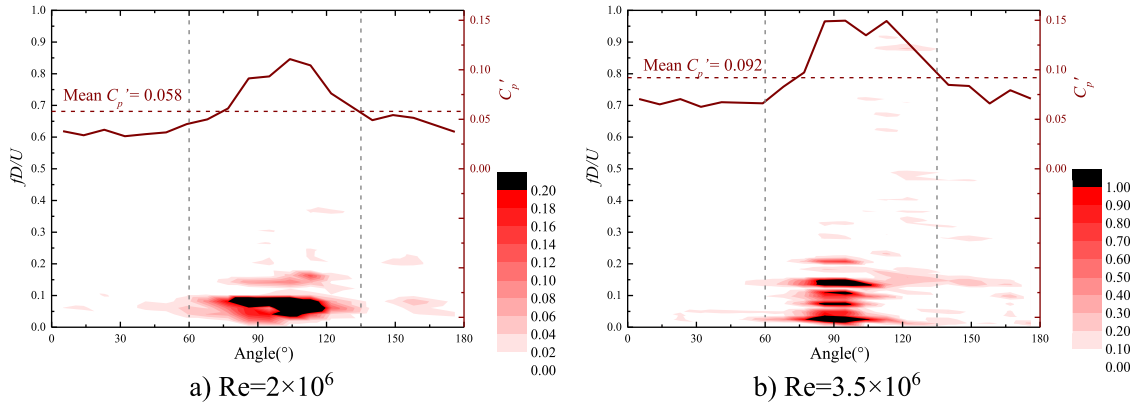

FIG. 10. C_p' and PSD of the surface pressure.

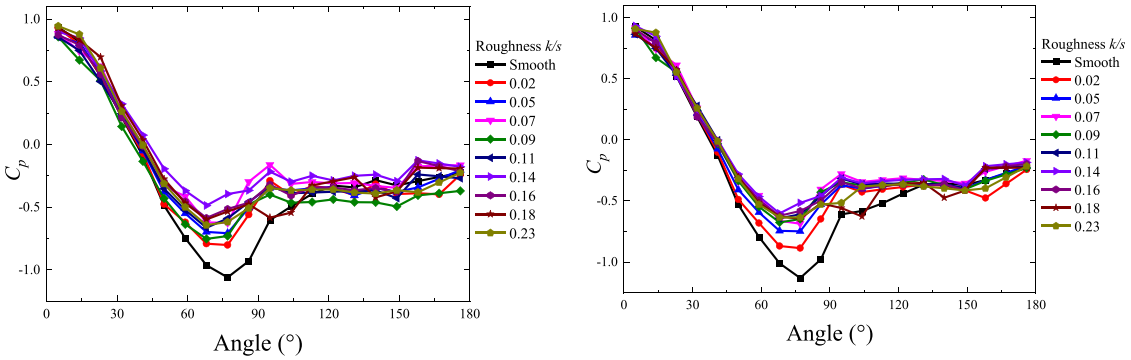

FIG. 11. C_p distribution under different equivalent roughness.

flow field characteristic points C_{pmin} and C_{pb}, and their corresponding positions θ_{min} and θ_{pb}. C_{pb} is defined as the mean value of C_p in the range within θ_{pb} to 180°. In general, $|C_{pmin}|$ decreases with the increase in roughness, from about −1.1 to −0.6, as shown in Fig. 12(a). When $\mathrm{Re} = 2 \times 10^6$, $|C_{pmin}|$ decreases with fluctuation, while C_{pmin} changes more smoothly for $\mathrm{Re} = 3.5 \times 10^6$ and becomes stable earlier. This shows that surface roughness can make the flow field enter the higher Re regime earlier. When the roughness reaches a certain value, the C_p distribution has almost no significant change with increasing roughness. It can be assumed that the flow field jumps from the supercritical regime to the transcritical regime, in which the C_p distribution is independent of the Re number. For $\mathrm{Re} = 3.5 \times 10^6$, after $k/s > 0.1$, C_{pmin} has become stable. For $\mathrm{Re} = 2 \times 10^6$, the corresponding k/s *is* higher than 0.15. Therefore, the flow field at higher Re could enter TrBL4 in advance at lower surface roughness. On the other hand, the effect of roughness on C_{pb} is not obvious. According to Fig. 12(b), although θ_{min} and θ_{pb} both move upstream, θ_{min} moves slightly with k/s higher than 0.08, while θ_{pb} varies greatly for about 130°–95° with one-layer roughness strip. The range of wake with stable C_{pb} was greatly expanded because the transition occurs at one of the first roughness strips. The specific transition position is not measured in this work, but the range can be roughly determined based on θ_{pb}. It indicates that the flow field in TrBL3 is very sensitive to disturbances. Under the first layer roughness strip, the flow separation and transition occur in advance by about 35° upstream. When $k/s > 0.18$, the C_p curve is relatively flat; it is difficult to determine the exact θ_{pb}, and θ_{pb} shows weak fluctuations.

The effect of the surface roughness seems to be inline with the conclusions of previous studies (Achenbach, 1968; Achenbach and Heinecke, 1981; and Zdravkovich, 1997), namely, the regime will change at lower Re numbers. On the other hand, surface roughness can be categorized into (a) uniform and dense roughness (sandpaper, glass beads, and knurled surfaces); (b) technical roughness with random variations in element size, shape, and spacing (concrete surfaces); and (c) discrete ribs and wires parallel to the cylinder axis. While comprehensive experimental data are available for most cases of the first type, the third category, which is the approach adopted in this study, still lacks systematic and thorough investigations into the effects of roughness variations. To address this limitation, experimental investigations from Niemann (1980) on cooling tower models with different rib-induced roughness levels are referred. Niemann (1980) investigated the distribution law of C_{pmin} and C_{pb} on cooling tower surface wind

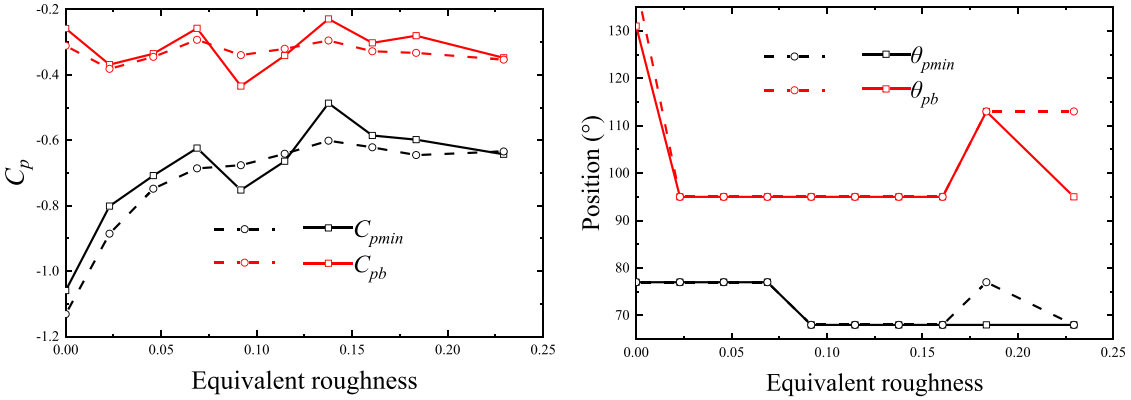

FIG. 12. Variation of flow field characteristic points with equivalent roughness: solid line: $\mathrm{Re} = 2 \times 10^6$, dashed line: $\mathrm{Re} = 3.5 \times 10^6$.

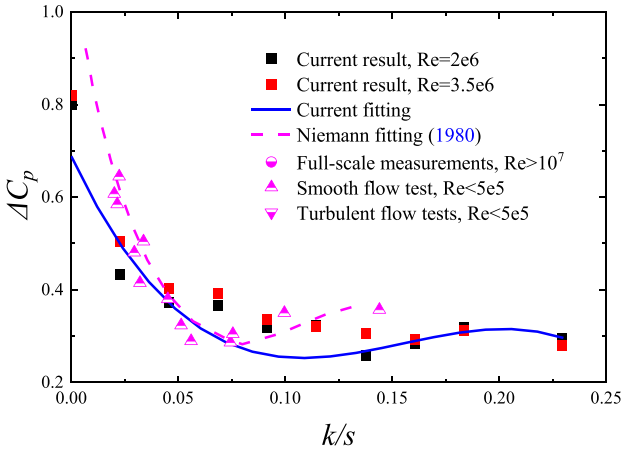

FIG. 13. Comparison of variation of ΔC_p with equivalent roughness.

pressure in the uniform flow and shear and proposed the relationship between the surface roughness and the pressure-rise coefficient ΔC_p defined as

$$\Delta C_p = C_{pb} - C_{pmin}. \tag{6}$$

Figure 13 shows the variation of ΔC_p with equivalent roughness at two Re in uniform flow, and compares the results with the fitting curve proposed by Niemann. Niemann's suggested curve includes different scaled model wind experiments ($Re < 5 \times 10^5$) and full-scale measurements of cooling towers ($Re > 10^7$), which implies a negligible Re effect on ΔC_p. Therefore, it can be roughly estimated that the impact of Re can be temporarily ignored. The fitting curve of ΔC_p obtained in this study is also given. Two fitting curves have good consistency in the interval $k/s = 0.02 - 0.1$. However, the fitting curve of the present results has a smaller slope and a more gentle change when $k/s < 0.02$ and $k/s > 0.1$. This discrepancy may be attributed to the limited data points in Niemann's study for $k/s > 0.1$, which contains only a single data point. Whereas for values below 0.02, Niemann's curve incorporates actual measurement data that is subject to more uncertainty factors, such as wind field characteristics in the atmospheric boundary layer and testing locations. Overall, the experimental results presented in this study regarding the effect of roughness on pressure distribution are reliable and credible.

Figure 14 gives fluctuating wind pressure C_p' distributions under different equivalent roughness at two Re numbers. The C_p' distribution is very sensitive to roughness. C_p' decreases sharply with one layer of roughness strip. Most C_p's are below 0.05 with the disappearance of the high platforms around 80°–110°. Only when $Re = 3.5 \times 10^6$ and $k/s =$ (0. 02, 0. 05, 0.23), there still remains some larger C_p' in the crosswind area. As mentioned earlier, compared with the smooth model, transition and separation of the flow field occur at one of the roughness strips near 95°, resulting in large vortex breaking into smaller ones, more energy dissipation, and, hence, lower turbulence fluctuation.

Figures 15 and 16 give C_p' and PSD of the wind pressure at $Re = 2 \times 10^6$ and $Re = 3.5 \times 10^6$ under four typical roughness, respectively. From $k/s = 0.02$–0.16, the C_p' distribution slightly moves downward, and PSD significantly decreases especially in the low-frequency range, which shows the turbulence energy is weakened by surface roughness. Moreover, C_p' curves are not as smooth as the smooth model and have large fluctuations. This may be due to the randomness of the flow field caused by roughness strips. When k/s is >0.1, the C_p distribution has almost no more changes as shown in Fig. 11, and the mean of C_p' is also the same at $k/s = 0.11$ and $k/s = 0.16$. However, from the point of view of PSD, the energy distribution is more concentrated at low frequency at $k/s = 0.11$, which indicates that the surface roughness of different heights still has some influence on the flow field characteristics. Therefore, if the inappropriate large roughness is used to simulate the Re effect in a scaled model experiment in order to produce a flow field in a super- or transcritical regime, the turbulent energy reduction effect caused by the roughness strip can result in the underestimation of C_p'.

Moreover, when $k/s = 0.23$, C_p' increases especially in the range of 60°–90° in the crosswind area, and this situation is more prominent at $Re = 3.5 \times 10^6$, which may be caused by the essential change of the local or global flow field under this large roughness. As shown in Figs. 16(c) and 16(d), under $Re = 3.5 \times 10^6$ conditions, when k/s increases from 0.16 to 0.23, the PSD across the entire angular range not only fails to decrease further but also shows a remarkable increase. Particularly in the 150°–180° region, the PSD also exhibits a substantial increase.

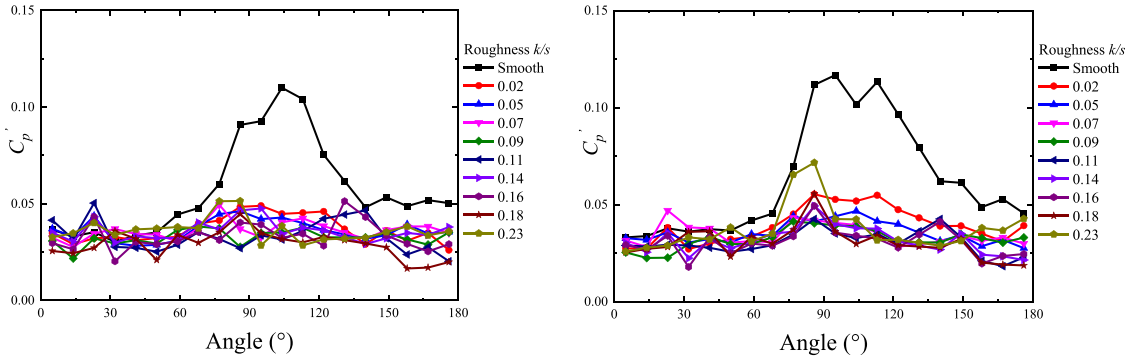

FIG. 14. C_p' distribution under different equivalent roughness.

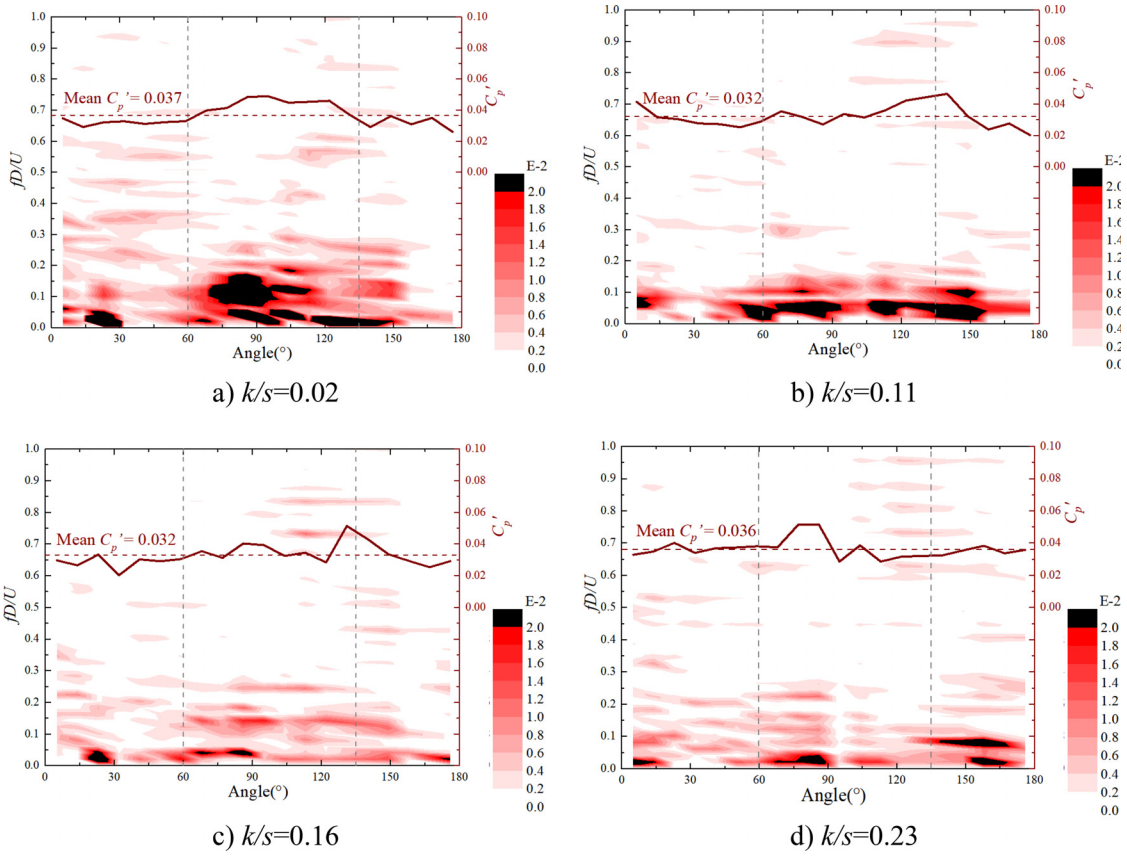

FIG. 15. C_p' and PSD of the wind pressure at $\mathrm{Re} = 2 \times 10^6$.

This results in prominent PSD peaks in the low-frequency range ($fD/U < 0.1$ and around 0.16) that span both the crosswind and wake regions, suggesting the possible reemergence of periodic vortex shedding, which is a primary characteristic of TrBL4. The early transition to TrBL4 at lower Re is, indeed, one of the effects of surface roughness. Although surface pressure on only half of the cylinder circumference was measured, preventing direct acquisition of lift time history, the existing PSD data clearly indicate the presence of regular vortex shedding in the flow field with fD/U around 0.16, slightly lower than values 0.2–0.3 reported in previous literature (Zdravkovich, 1997), which might be attributed to the influence of surface roughness and aspect ratio.

C. Incoming turbulence effect

Figure 17 gives C_p distributions with the turbulence intensity on the smooth and three equivalent rough surfaces at $\mathrm{Re} = 2 \times 10^6$. The general trend of C_p distributions under different surface conditions is the same, that is, C_{pmin} and C_{pb} decrease with the increase in I_u. With the increase in roughness, C_p curves corresponding to different I_u become closer. Especially, when $k/s = 0.23$, except $I_u = 15\%$, the C_p curves corresponding to the other three turbulent flows are very close to the one corresponding to the smooth model. This shows that the incoming turbulence effect is weakened by roughness. Figure 18 shows the variation of flow field characteristic points C_{pmin} and C_{pb}, and their corresponding positions θ_{min} and θ_{pb} with different equivalent roughness and incoming turbulence. The variation trends in the four turbulent flows are similar to those under uniform flow. θ_{min} fluctuates around 68°, and θ_{pb} moved from around 130° to 90° with the first layer roughness strip. It can be inferred that the incoming turbulence mainly influences the values of C_{pmin} and C_{pb}, while the whole distribution, such as the position of characteristic points θ_{min} and θ_{pb}, is more affected by surface roughness. The results at $\mathrm{Re} = 3.5 \times 10^6$ are similar to those at $\mathrm{Re} = 2 \times 10^6$ and are not repeated in this paper.

Figure 19 gives the variation of C_p' curves at $\mathrm{Re} = 2 \times 10^6$ with different k/s and I_u. Under each k/s, C_p' curves move upward with the increase in I_u, but the distributions are different under changing I_u. The C_p' curve of the smooth cylinder in a uniform flow field has an obvious plateau, covering 90°–120°. In the turbulent flow, when I_u is small, i.e., 4% and 7%, C_p' increases but remains below 0.1 with a small peak in the crosswind area for smooth and rough surfaces. Under these conditions, the C_p' distribution is similar to that under uniform flow, so lower incoming turbulence has no obvious effect on the C_p' distribution of the rough model. When $I_u = 10\%$, C_p' curves have two maxima around the stagnation point and 100° for surfaces of smooth, and $k/s = 0.02$. When $I_u = 15\%$, C_p' shows greater fluctuations for low roughness, i.e., smooth and $k/s = 0.02$. With the roughness increase as shown in Fig. 19(c) when $k/s = 0.11$, C_p' is relatively flat with a continuous,

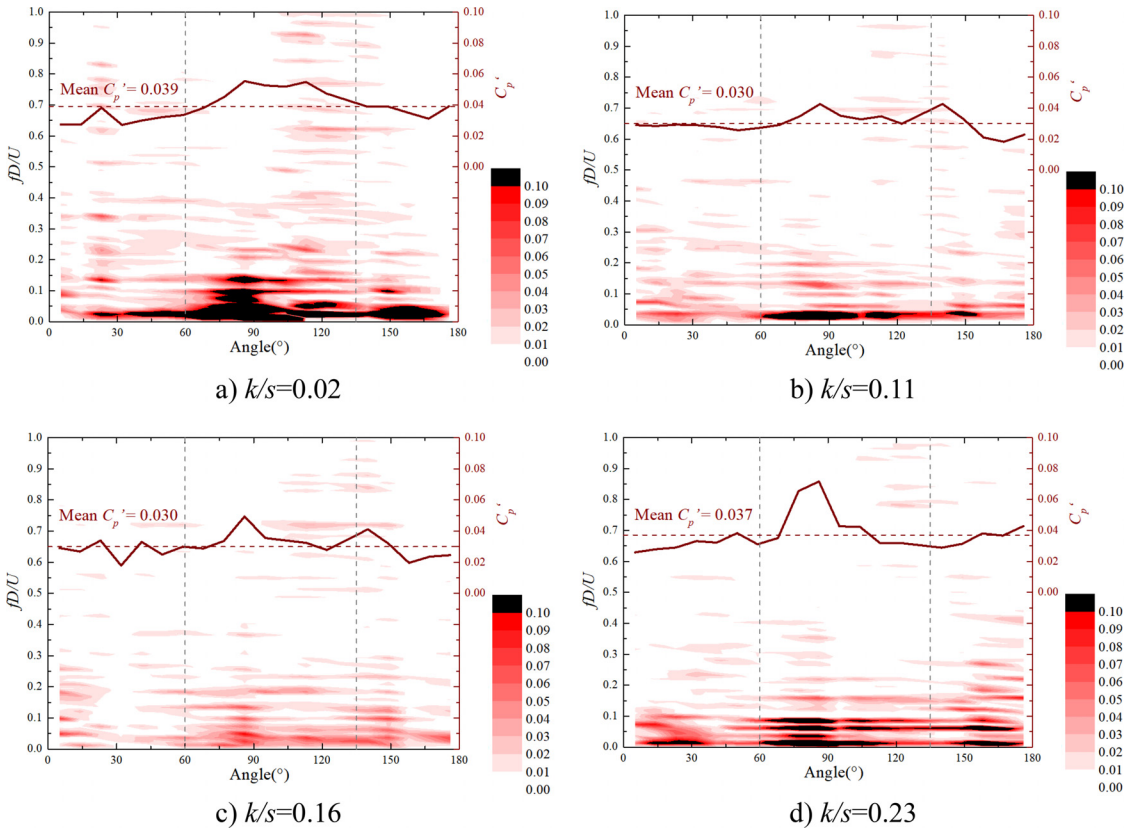

FIG. 16. C_p' and PSD of the wind pressure at Re = 3.5×10^6.

steady small decrease. The maximum crosswind area disappears, which may be caused by higher rough strips. Additionally, the curve looks unusual fluctuation in the crosswind area, and this may also be related to the vortex fragmentation by rough strips and more turbulent energy dissipation of smaller vortex. When $k/s = 0.23$, which is the maximum roughness of this experiment, the maximum in uniform and the turbulent flow all move upstream around 80°–90° under the large roughness effect. The curves are similar in distribution and closer to each other.

In general, in the uniform flow, the value of C_p' is <0.1 for all roughness conditions. Turbulence significantly alters the magnitude and trend of C_p'. As the roughness increases, the difference in C_p' between rough and smooth surfaces diminishes, which implies that the attenuating and disturbing effects of roughness on C_p' are similarly manifested in the influence of incoming turbulence. Again, there may be a problem of distorted C_p' curve when simulating the Re effect by adding surface roughness on the scaled model, and the scaled model results obtained by rough models need to be verified carefully.

Figure 20 gives the variation of the maximum value of the two maximum areas at the stagnation point and the crosswind area with the equivalent roughness k/s. C_{ps}' is the maximum C_p' around the stagnation point, and C_{pmax}' is the maximum C_p' in the crosswind area. C_{ps}' is less affected by the roughness, fluctuating around the C_p' of the smooth surface model. This may be because the flow field at the stationary point has not been disturbed by the roughness strips yet. On the other hand, with the increase in roughness, C_{pmax}' decreases rapidly. When the equivalent roughness $k/s > 0.05$, C_{pmax}' under each larger surface roughness almost remains unchanged. When I_u=15% as shown in Fig. 20(d), C_{ps}' fluctuates greatly with higher roughness. The possible reason is that when the turbulence intensity is high enough, the flow field is interfered with by both roughness and turbulence, and the combining effect is more complicated as it is also influenced by turbulence characteristics, such as turbulent integral scale and power spectrum.

D. Probabilistic characteristics of fluctuating pressure

As previously discussed, both surface roughness and incoming turbulence significantly influence wind pressure distribution, albeit through distinct mechanisms. This section delves deeper into these influences from a probabilistic statistical perspective. The wind pressure acting on a structural surface can be conceptually modeled as the superposition of numerous vortices of varying scales within the flow field. When the structural surface area is sufficiently large, the probabilistic correlation between different spatial points in the flow field diminishes, allowing each vortex in the spatial domain to be treated as statistically independent. By the central limit theorem, the superposition of a sufficiently large number of independent random variables tends toward a Gaussian distribution.

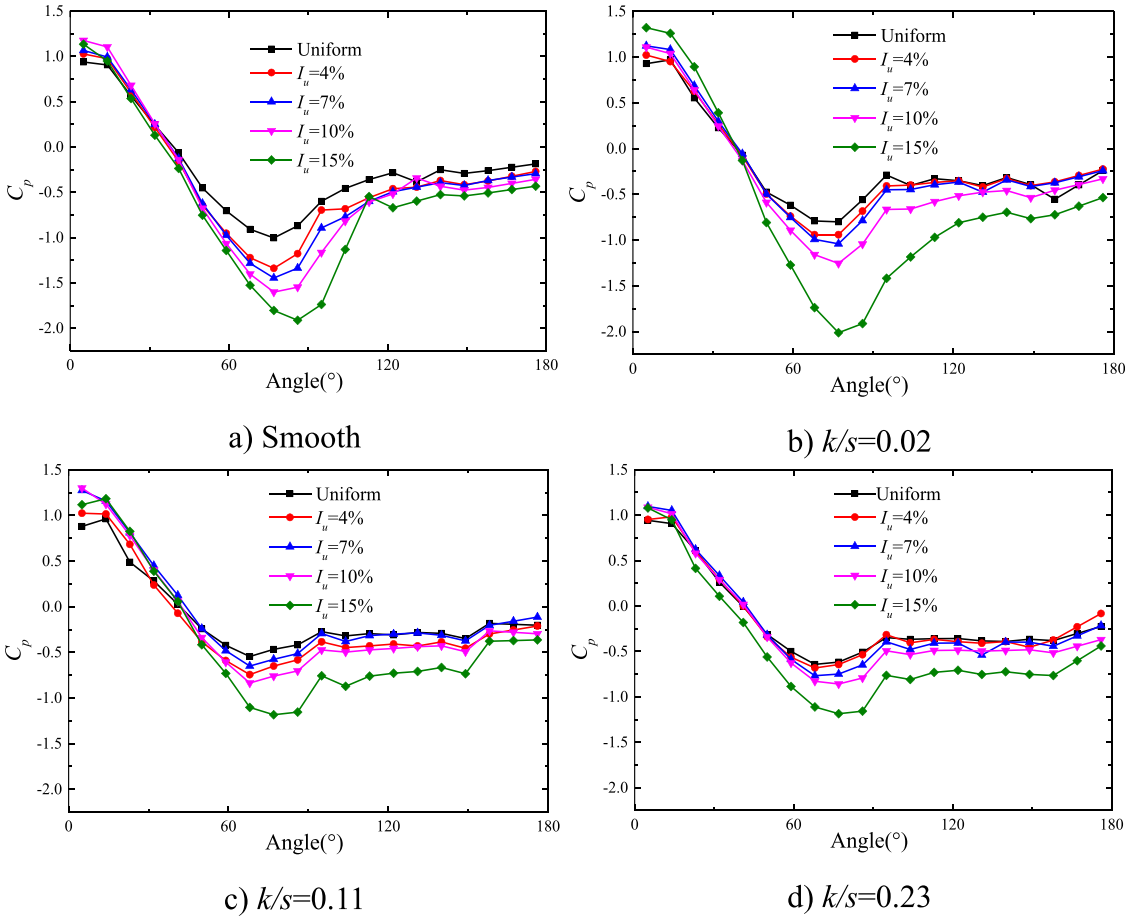

FIG. 17. C_p distribution under different equivalent roughness and incoming turbulence.

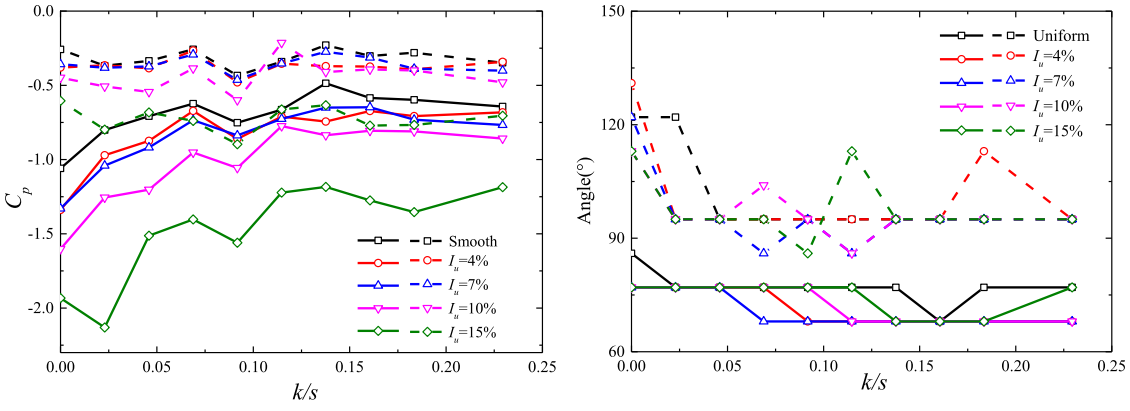

FIG. 18. Variation of flow field characteristic points with equivalent roughness and incoming turbulence, $\mathrm{Re} = 2 \times 10^6$.

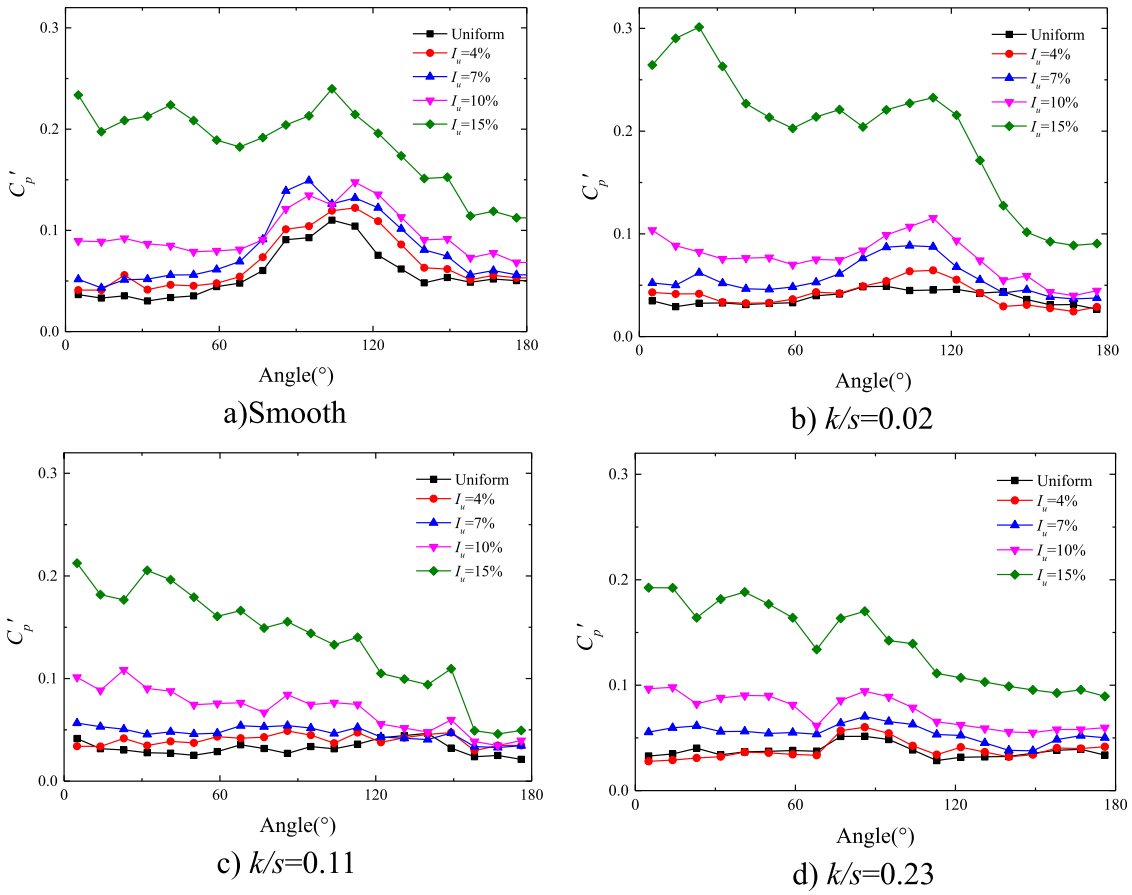

FIG. 19. C_p' distribution under different equivalent roughness and turbulence.

Conversely, when organized vortex structures dominate a local region, resulting in strong spatial correlations, the fundamental assumptions of the central limit theorem are no longer satisfied. Consequently, the wind pressure signals exhibit non-Gaussian characteristics. The wind pressure time series in non-Gaussian regions are asymmetrically distributed and are accompanied by large amplitude wind pressure pulses. These repeated pulses can often lead to local damage.

The first- and second-order statistics cannot accurately describe the Gaussian distribution characteristics, so the third- and fourth-order statistics, called skewness S_k and kurtosis K_u, need to be introduced as

$$S_k = E\left[\frac{\left(C_{pi}(t) - \overline{C_{pi}}\right)^3}{C_{pi}}\right], \tag{7}$$

$$K_u = E\left[\frac{\left(C_{pi}(t) - \overline{C_{pi}}\right)^4}{C_{pi}}\right], \tag{8}$$

where $C_{pi}(t)$ is the wind pressure time history, which is normalized using $C_{p\_N} = (C_p(t) - C_p)/C_p'$. For a standard Gaussian distribution, $S_k = 0$ and $K_u = 3$. The more S_k and $K_u - 3$ deviate from zero, the stronger the non-Gaussian. Figure 21 shows probability density distributions at the characteristic points of the smooth cylinder in uniform flow at $\mathrm{Re} = 2 \times 10^6$. The wind pressure history at the stagnation and wake points has weak non-Gaussian characteristics, while the negative pressure extreme and the separation points may show relatively strong non-Gaussian behavior.

In addition to S_k and K_u, the Kolmogorov–Smirnov (KS) test was employed to assess whether the wind pressure distributions conform to a Gaussian distribution. The KS test is a non-parametric statistical method used to determine if a sample originates from a specific theoretical distribution. Its fundamental principle involves comparing the empirical cumulative distribution function (ECDF) of the sample with the cumulative distribution function (CDF) of the theoretical distribution, using the maximum discrepancy between them to decide whether to reject the null hypothesis. This test is widely applied in normality testing, residual distribution analysis in regression models, and goodness-of-fit testing for extreme event distributions. Figure 22 presents S_k and K_u values for a smooth surface at $\mathrm{Re} = 2 \times 10^6$ under varying incoming turbulence conditions. The figure also highlights the S_k–K_u region identified as Gaussian-distributed by the KS test, shaded in red, with the range $-0.19 < S_k < 0.13$ and $2.7 < K_u < 3.7$. This region encompasses over 95% of the Gaussian-distributed cases. As illustrated

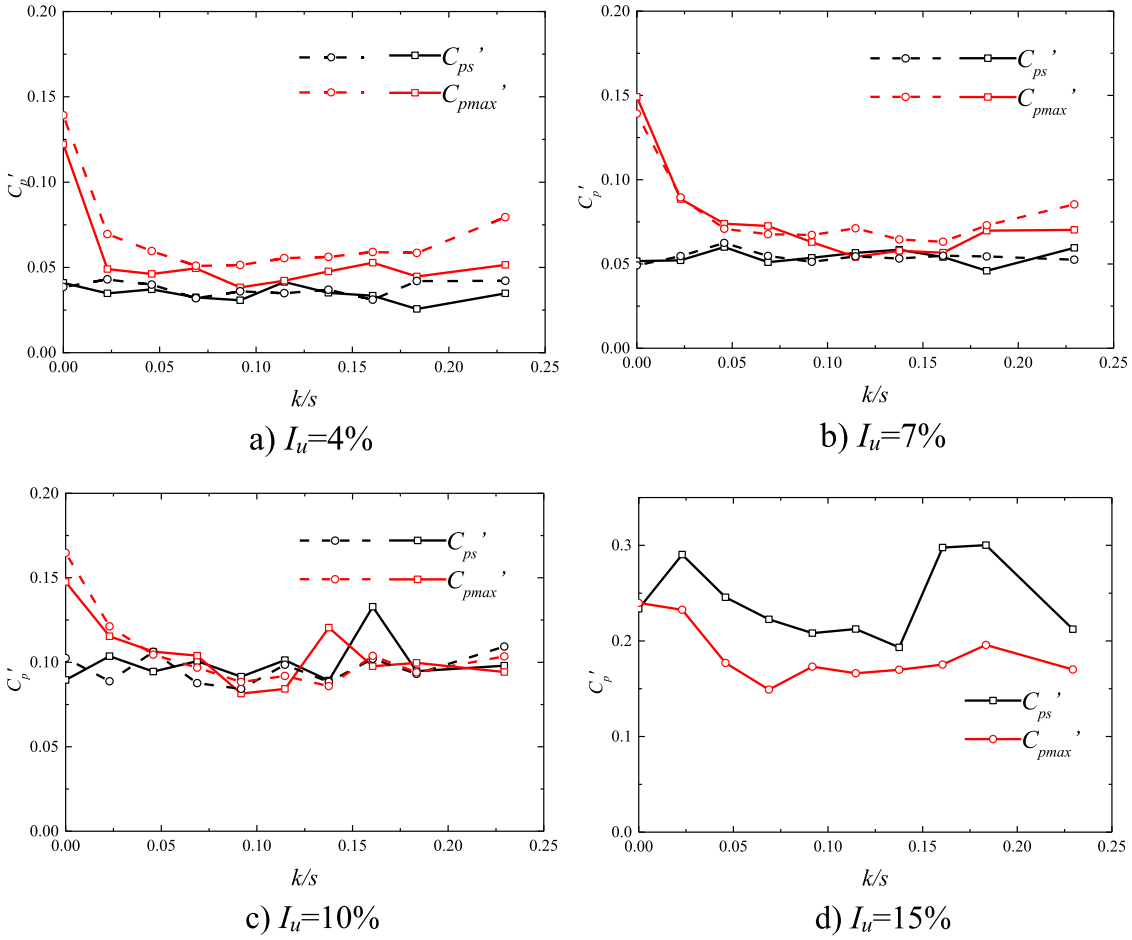

FIG. 20. Variation of C_{ps}' and C_{pmax}' with the equivalent roughness k/s: solid line: $\mathrm{Re} = 2 \times 10^6$ and dashed line: $\mathrm{Re} = 3.5 \times 10^6$.

in Fig. 22(a), under both uniform and turbulent flow conditions, some measurement points exhibit non-Gaussian characteristics, with stronger non-Gaussian behavior observed in turbulent flows. At $I_u = 4\%$, the K_u values of the measurement points show significant variation, while at $I_u = 10\%$ and 15%, S_k values exhibit greater divergence. Figure 22(b) shows the variation of S_k and K_u with circumferential angle. S_k and K_u values at the stagnation point differ considerably, likely due to the inherent non-Gaussian nature of the incoming turbulence itself. Except for $I_u = 7\%$ and 10%, the trends of S_k and K_u for the remaining cases are similar. Under turbulent conditions, wind pressure time histories with pronounced non-Gaussian characteristics can emerge in all regions, with high S_k and K_u values typically not co-occurring at the same point, contrasting with the characteristics observed in the critical Re regime (Chang *et al.*, 2022).

Figure 23 shows the S_k and K_u values for each measurement point on rough surfaces at $\mathrm{Re} = 2 \times 10^6$ under different incoming turbulence conditions. The region identified as Gaussian-distributed by the KS test is similarly shaded in red. This region varies slightly across different roughness levels, with the S_k lower limit ranging from −0.15 to −0.17 and the upper limit ranging from 0.17 to 0.2. The K_u lower limit is approximately 2.7, while the upper limit ranges between 3.5 and 3.7. Compared with uniform flow, the incoming turbulence increases the number of measuring points with non-Gaussian distribution, and the non-Gaussian characteristics become stronger. With the increase in roughness, the wind pressure of each measuring point gradually converges to the approximate Gaussian distribution area, indicating that roughness weakens the non-Gaussian characteristics caused by the incoming turbulence. However, the non-Gaussian characteristics caused by larger turbulence are still obvious. As shown in Fig. 23(c), when $k/s = 0.16$, almost all measuring points in the uniform flow do not show non-Gaussian, while there are many non-Gaussian points with large S_k in turbulent flow of $I_u = 10\%$ and 15%.

Large-scale structural vortices can not only improve the non-Gaussian characteristics but also enhance the spatial correlation. The correlation coefficient r is an important index to evaluate the correlation of two signal sequences, expressed as

$$r(X, Y) = \frac{Cov(X, Y)}{\sqrt{Var[X]Var[Y]}}, \tag{9}$$

where $Cov(X, Y)$ represents the covariance of two sequences, $Var[X]$ and $Var[Y]$ are the variance of X and Y, respectively. Figure 24

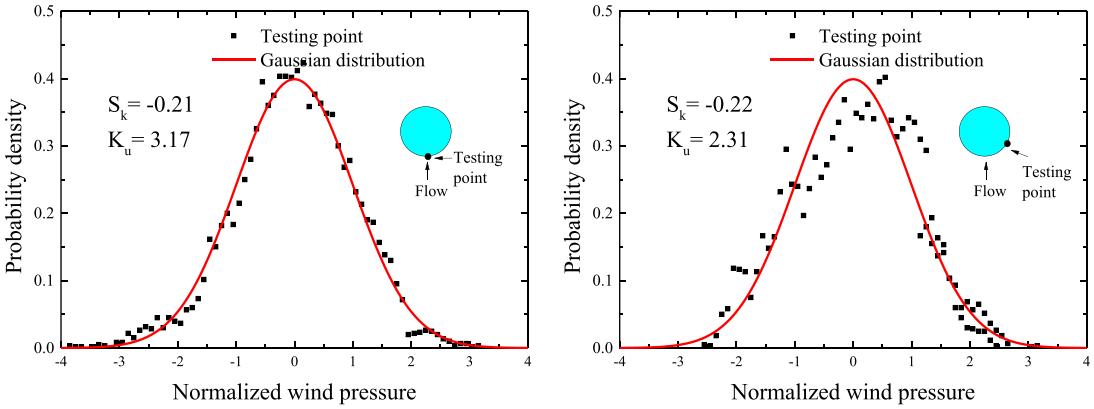

a) Stagnation point, θ=0° b) Negative pressure extreme point, θ_{pmin}=77°

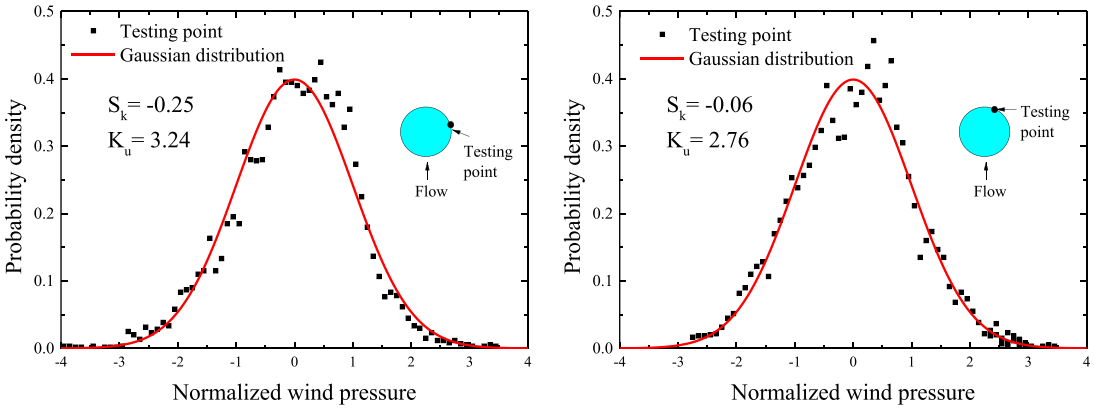

c) Flow separation point, θ_{pb}=122° d) Wake point, θ=158°

FIG. 21. Probability density distribution of characteristic points (Re = 2×10^6).

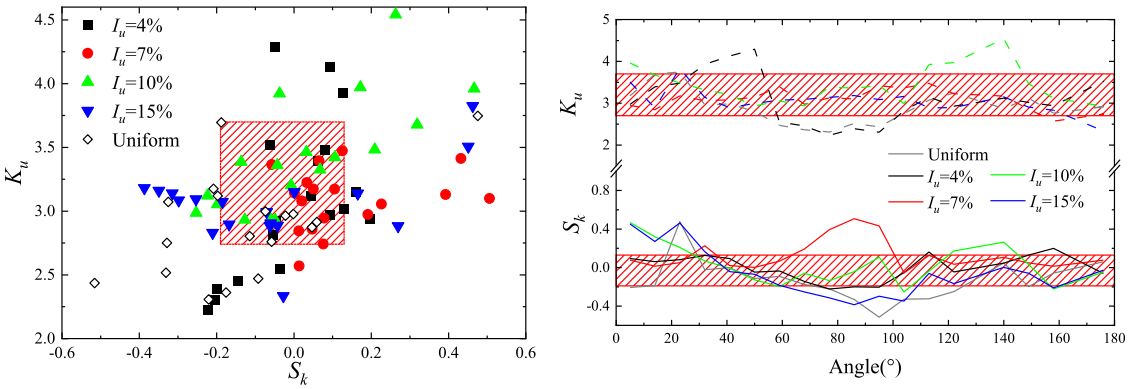

a) S_k-K_u diagram for all circumferential points b) S_k and K_u change with angle

FIG. 22. S_k and K_u for smooth cylinder (Re = 2×10^6).

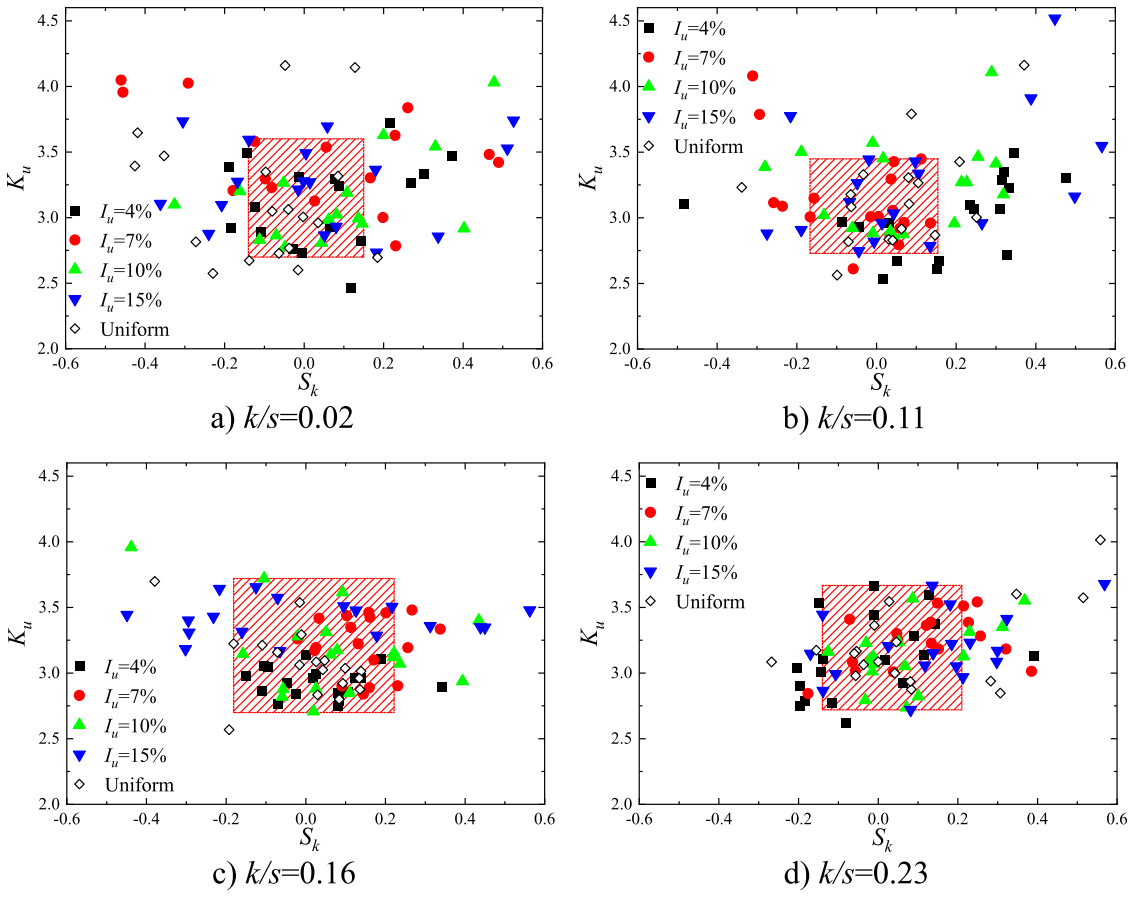

FIG. 23. S_k–K_u diagram for all circumferential points with surface roughness (Re = 2×10^6).

shows the spatial correlation at the separation point of the rough surface, which is the position with strong non-Gaussianity. It can be seen that as the roughness increases, the correlation coefficient decreases rapidly. In particular, when $k/s \geq 0.16$, except for the separation point at 95°, the correlation coefficients at other measurement points are generally <0.55. This value can be regarded as a reference indicator for the impact of roughness on vortex correlation. The area with values >0.55 is considered a strongly correlated area, while values <0.55 indicate moderately to weakly correlated areas, where the influence of roughness on the flow field vortex structure is no longer significant. The black stripes represent the actual location of the roughness strips, and the blue background represents the angle range with a strong correlation.

It is evident that as roughness increases, the strongly correlated region diminishes from approximately 25° (70°–105°, covering eight roughness strips) near the separation point to a narrower 5°–10° region (90°–100°, covering one to two roughness strips). This reduction indicates that the roughness strips disrupt the large-scale vortices. When $k/s \geq 0.16$, the vortex correlation sharply decreases after passing through the roughness strips, consistently remaining below 0.55. It can be inferred that when the roughness strips are sufficiently high, most of the turbulence exists in the form of very small-scale vortices confined between two roughness strips. Consequently, further increasing the height of the roughness has a negligible impact on the flow field and pressure. This also suggests that roughness strips with the same equivalent roughness but different spacing arrangements may still influence the flow field.

The incoming turbulence has a certain effect on enhancing the structural vortex in the flow field, but its enhancing effect on the spatial correlation coefficient is mainly in the medium value area of 0.2–0.5, while the effect on the strong correlation area can be ignored. According to Table I, the integral scale range of the four turbulent flows is 30–60 cm, which is approximately 1.5–3 times the roughness strip interval. This type of small vortex structure of incoming turbulence is easily fragmented due to the interference of roughness stripes, which may be the reason why turbulence intensity has a relatively small impact on a strong correlation area.

Figure 25 shows a strong correlation range between the separation point and other locations, with one scale representing one spacing between roughness strips under different surface conditions and incoming flow conditions. It can be seen that on a smooth surface, the strong correlation range is essentially within six to ten roughness strip spacings, approximately 30°–50°. At lower surface roughness, i.e., $k/s \leq 0.04$, the strong correlation area is essentially within four to six

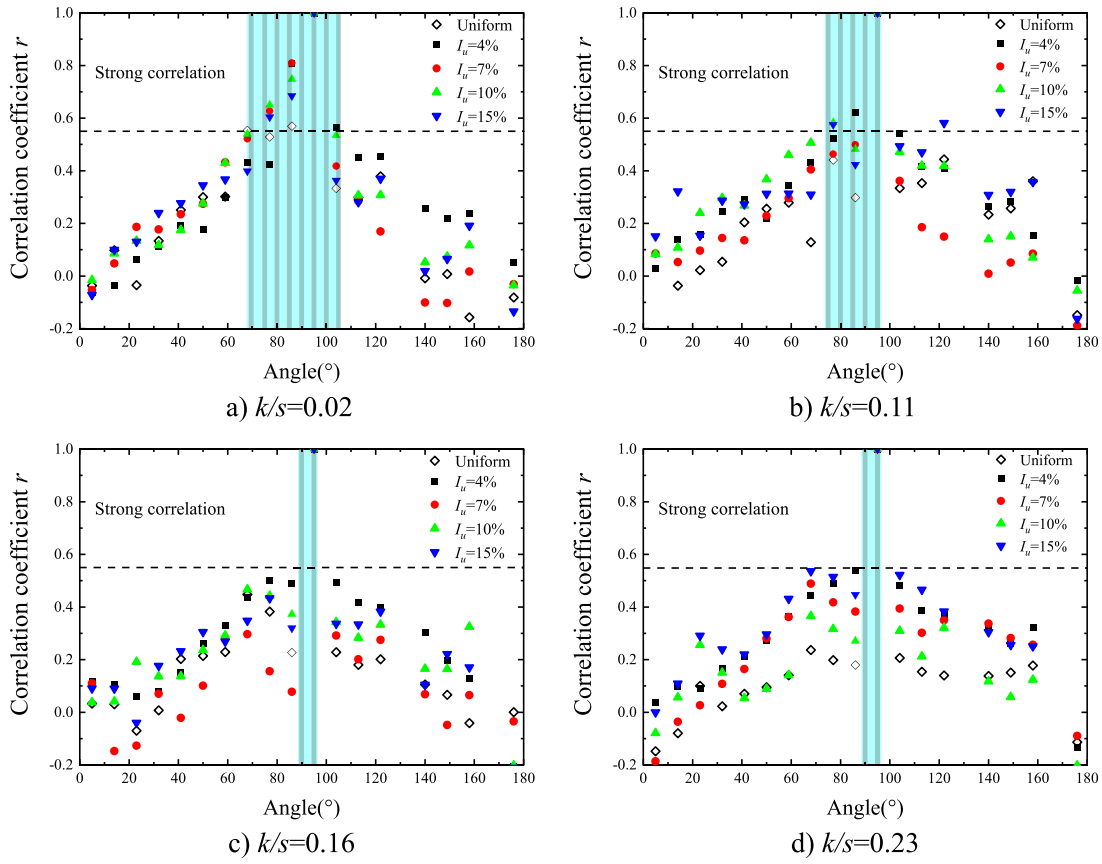

FIG. 24. Spatial correlation between the separation point and other locations at rough surfaces, Re = 2×10^6.

roughness spacings, approximately 20°–30°. As the roughness continues to increase, the strong correlation area rapidly decays. For uniform flow and $I_u \leq 10\%$, the strong correlation range is essentially reduced to one roughness strip spacing after the roughness exceeds 0.07. When $I_u = 15\%$ and $k/s \geq 0.07$, the strong correlation range fluctuates within one to four roughness spacings, indicating that the incoming flow characteristics under high turbulence still have a certain dominant effect on the flow field. The spatial correlation of wind pressure primarily reflects the influence of large-scale organized vortices on the structural surface. The reduction in the strongly correlated region suggests that the influence range of such vortices decreases from six to ten times the characteristic scale of roughness strips on smooth surfaces to approximately one time on highly rough surfaces. This observation further confirms that roughness strips disrupt vortices and attenuate turbulent energy. While incoming turbulence can enhance large-scale vortices, its effect is also modulated by surface roughness. Therefore, when using roughness to simulate high Reynolds number effects, special attention should be paid to the distortion of the turbulent flow field and fluctuating pressure.

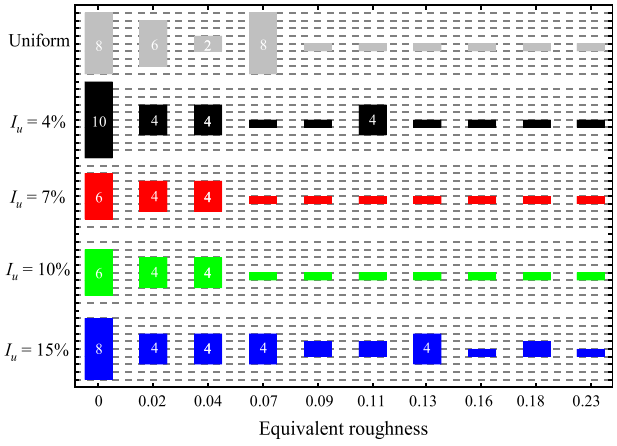

FIG. 25. Strong correlation coverage range between the separation point and other locations, with one scale representing one spacing between roughness strips, Re = 2×10^6.

IV. CONCLUSIONS

A novel distributed synchronous force measurement system has been developed, which is capable of measuring the surface wind load of large-scale structural models. The advantage of this system lies in its ability to avoid signal distortion issues caused by the excessively long tubes of the pressure measurement system. Utilizing this system, the flow around a short cylinder model under a supercritical Re regime was replicated in a large atmospheric boundary layer wind tunnel. The

effects of roughness and incoming turbulence on the wind load were investigated.

The experimental results indicate that both roughness and turbulence significantly alter the flow pattern, albeit through different mechanisms. Roughness induces an early transition to turbulence at the location of the roughness strips, leading to a significant change in the mean wind pressure curve. Concurrently, due to the breakup of large-scale vortices, the turbulence energy is diminished, resulting in a notable reduction in fluctuating wind pressure. The incoming turbulence also modifies the mean wind pressure but has a minimal impact on its circumferential trend. The signature turbulence of the flow around a cylinder in uniform flow is overshadowed by the features of the incoming turbulence. As the turbulence intensity increases, the fluctuating wind pressure curve shifts upward, with two regions of maximum values in the stagnation and crosswind areas. The effect of turbulence on wind pressure is also influenced by the roughness strips; as the roughness increases, the difference in *Cp'* between the rough and smooth surfaces decreases. The probabilistic statistical characteristics of wind pressure time series are also influenced by incoming turbulence and roughness. In general, turbulence tends to increase non-Gaussian characteristics, while roughness has the opposite effect, and the two interact with each other. Based on the correlation analysis of wind pressure time series, it can be inferred that the influence range of large-scale structural vortices is significantly reduced on highly rough surfaces compared to smooth surfaces, decreasing from approximately six to ten times the characteristic scale of roughness strips to about one time. This implies that when simulating the Re effect by adding surface roughness to scaled models, distortions in the fluctuating wind pressure curve may occur, necessitating careful verification of the results obtained from the roughness model on the scaled model.

ACKNOWLEDGMENTS

The authors gratefully acknowledge the support of the National Key Research and Development Program of China (2022YFC3005301), the National Natural Science Foundation of China (52308514), and the Sichuan Science and Technology Program (2024NSFSC0931).

AUTHOR DECLARATIONS

Conflict of Interest

The authors have no conflicts to disclose.

Author Contributions

Ying Chang: Data curation (equal); Formal analysis (equal); Investigation (equal); Methodology (equal); Writing – original draft (equal). **Lin Zhao:** Data curation (equal); Formal analysis (equal); Writing – review & editing (equal). **Yangzhao Liu:** Conceptualization (equal); Investigation (equal); Supervision (equal); Writing – review & editing (equal). **Haili Liao:** Conceptualization (equal); Investigation (equal); Supervision (equal). **Yaojun Ge:** Conceptualization (equal); Investigation (equal); Supervision (equal).

DATA AVAILABILITY

The data that support the findings of this study are available from the corresponding author upon reasonable request.

REFERENCES

Abdelhadya, M. and Wood, D., "An investigation of the wakes of stranded cables using particle image velocimetry," Phys. Fluids **33**, 035132 (2021).
Achenbach, E., "Distribution of local pressure and skin friction around a circular cylinder in cross-flow up to $Re = 5 \times 10^6$," J. Fluid Mech. **34**(4), 625–639 (1968).
Achenbach, E. and Heinecke, E., "On vortex shedding from smooth and rough cylinders in the range of Reynolds numbers 6×10^3 to 5×10^6," J. Fluid Mech. **109**(106), 239–251 (1981).
Bearman, P. W. and Morel, T., "Effect of free stream turbulence on the flow around bluff bodies," Prog. Aerosp. Sci. **20**, 97–123 (1983).
Bergh, H. and Tijdeman, H., *Theoretical and Experimental Results for the Dynamic Response of Pressure Measuring Systems*. NLR-TR F. 238 (Nationaal Lucht-en Ruimtevaartlaboratorium, 1965).
Chang, Y., Zhao, L., Chen, L. *et al.*, "Effect of free stream turbulence in critical Reynolds number regime (1.6×10^5–6.1×10^5) on flow around circular cylinder," Phys. Fluids **34**(11), 115126 (2022).
Chen, C. H., Chang, C. H., and Lin, Y. Y., "The influence of model surface roughness on wind loads of the RC chimney by comparing the full-scale measurements and wind tunnel simulations," Wind Struct. **16**(2), 137–156 (2013).
Flay, R. G. J. and Stevenson, D. C., "Integral length scales in strong winds below 20 m," J. Wind Eng. Ind. Aerodyn. **28**(1–3), 21 (1988).
GB/T 50102-2014, *Industrial Circulating Water Cooling Design Specification* (China Planning Press, Beijing, China, 2014).
He, Y., Liang, Q., Li, Z., Fu, J., Wu, J., and Deng, T., "Accurate estimation of tube-induced distortion effects on wind pressure measurements," J. Wind Eng. Ind. Aerodyn. **188**, 260–268 (2019).
Holmes, J. and Lewis, R., "Optimization of dynamic-pressure-measurement systems. I. Single point measurements," J. Wind Eng. Ind. Aerodyn. **25**(3), 249–273 (1987a).
Holmes, J. and Lewis, R., "Optimization of dynamic-pressure-measurement systems. II. Parallel tube-manifold systems," J. Wind Eng. Ind. Aerodyn. **25**(3), 275–290 (1987b).
Hwang, Y., Shim, J., Kwon, O. S. *et al.*, "Real-time aeroelastic hybrid simulation method for a flexible bridge deck section model," J. Struct. Eng. **150**(10), 04024149 (2024).
Irwin, H., Cooper, K., and Girard, R., "Correction of distortion effects caused by tubing systems in measurements of fluctuating pressures," J. Wind Eng. Ind. Aerodyn. **5**(1–2), 93–107 (1979).
JGJ/T 338-2014, *Standard for Wind Tunnel Test of Buildings and Structures* (Ministry of Housing and Urban-Rural Development of the People's Republic of China, Beijing, China, 2014).
Jones, G. W., Cincotta, J., and Walker, W., "Aerodynamic forces on a stationary and oscillating circular cylinder at high Reynolds number," Technical Report TR R-300 (NASA, 1969), pp. 1–62.
Kay, N., Oo, N., Gill, M., Richards, P., and Sharma, R., "Robustness of the digital filter to differing calibration flows," J. Wind Eng. Ind. Aerodyn. **197**, 104061 (2020).
Khabbouchi, I., Fellouah, H., Ferchichi, M., and Guellouz, M. S., "Effects of free-stream turbulence and Reynolds number on the separated shear layer from a circular cylinder," J. Wind Eng. Ind. Aerodyn. **135**, 46–56 (2014).
Li, H. Y., Xu, Y. L., Wang, B. *et al.*, "Establishment and application of a digital twin for vortex-induced vibration of a bridge deck section," Eng. Appl. Comput. Fluid Mech. **18**(1), 2297032 (2024).
Liu, L., Sun, Y., Su, N., Wu, Y., and Peng, S. T., "Three-dimensional Reynolds number effects and wind load models for cylindrical storage tanks with low aspect ratios," J. Wind Eng. Ind. Aerodyn. **227**, 105080 (2022).
Ma, W. Y., Huang, B. C., Zheng, D. Q., Lu, M., and Li, H. Y., "Effect of the presence of end plates and aspect ratio on the aerodynamic forces on circular cylinders in various flow regimes," Fluid Dyn. Res. **51**, 055503 (2019a).
Ma, W. Y., Liu, Q. K., and Matsumoto, M., "Excitation of the large-amplitude vibrations of a circular cylinder under normal wind conditions in the critical Reynolds number range," J. Fluids Struct. **84**, 318–328 (2019b).
Maryami, R., Ali, S., Azarpeyvand, M., and Afshari, A., "Turbulent flow interaction with a circular cylinder," Phys. Fluids **32**(1), 015105 (2020).
Mctavish, S., D'Auteuil, A., and Raeesi, A., "Effect of cable surface characteristics and flow turbulence on the aerodynamic behaviour of stay cables in dry conditions," J. Wind Eng. Ind. Aerodyn. **207**, 104414 (2020).

Niemann, H. J., "Wind effects on cooling-tower shells," J. Struct. Div., Am. Soc. Civ. Eng. **106**(ST3), 643–661 (1980).
Pallas, N.-P., Kellaris, K., and Bouris, D., "Dynamic calibration of complex tubing systems using a single pressure measurement device," J. Wind Eng. Ind. Aerodyn. **249**, 105715 (2024).
Roshko, A., "Experiments on the flow past a circular cylinder at very high Reynolds number," J. Fluid Mech. **10**(3), 345–356 (1961).
Schewe, G., "On the force fluctuations acting on a circular cylinder in cross flow from subcritical up to transcritical Reynolds numbers," J. Fluid Mech. **133**, 265–285 (1983).
Surry, D., "Some effects of intense turbulence on the aerodynamics of a circular cylinder at subcritical Reynolds number," J. Fluid Mech. **52**, 543 (1972).
Van Numen, J. W. G., "Pressure and forces on a circular cylinder in a cross flow at high Reynolds numbers," in *Flow Induced Structural Vibrations*, edited by E. Naudascher (Springer, Berlin, 1974), pp. 748–754.
Wang, H. F., Zhou, Y., and Mi, J., "Effects of aspect ratio on the drag of a wall-mounted finite-length cylinder in subcritical and critical regimes," Exp. Fluids **53**, 423–436 (2012).
Yan, L., Li, J., He, X., and Li, Y., "Ride comfort assessment of road vehicles on a long-span truss girder suspension bridge under crosswinds," Eng. Struct. **322**, 119112 (2025).
Zan, S. J., "Experiments on circular cylinders in crossflow at Reynolds numbers up to 7 million," J. Wind Eng. Ind. Aerodyn. **96**(6–7), 880–886 (2008).
Zdravkovich, M. M., *Flow Around Circular Cylinders* (Oxford University Press, Oxford, UK, 1997), Vol. 1.
Zhao, L., Chen, H. L., Hu, X. N., and Ge, Y. J., "Distribution pattern of fluctuating wind pressures on cooling towers in grouped rectangular arrangement," J. Wind Eng. Ind. Aerodyn. **224**, 104975 (2022).
Zhu, L., Meng, X., and Guo, Z., "Nonlinear mathematical model of vortex-induced vertical force on a flat closed-box bridge deck," J. Wind Eng. Ind. Aerodyn. **122**, 69–82 (2013).